Journal of Materials Chemistry A

PAPER

View Article Online
View Journal | View Issue

Cite this: J. Mater. Chem. A, 2019, 7, 12489

Co_xFe_yN nanoparticles decorated on graphene sheets as high-performance electrocatalysts for the oxygen evolution reaction†

Haixia Liu,[a] Xinyao Lu,[a] Yi Hu,[a] Renpeng Chen,[a] Peiyang Zhao,[a] Lei Wang,[a] Guoyin Zhu,[a] Lianbo Ma [a] and Zhong Jin *[ab]

Exploring highly efficient non-noble metal based catalysts for the oxygen evolution reaction (OER) is of great importance for the development of renewable energy conversion technologies, such as water-splitting devices and rechargeable metal–air batteries. Co-based electrocatalysts have been regarded as a class of highly active and earth-abundant catalysts for the OER, but most of them are semiconductors or insulators that may limit the OER efficiency. Herein, we report the facile preparation of Co_xFe_yN nanoparticles uniformly loaded on graphene sheets (Co_xFe_yN/graphene) with amazing OER activity and stability, attributed to the intrinsic metallic characteristics. Through partial Fe heteroatom substitution in Co_4N lattices, the disorder of the crystalline structure could be increased, thus forming a more favorable electronic structure for the catalysis of the OER. By adjusting the atomic ratios of Co/Fe elements, we found that the Co_3Fe_1N/graphene catalyst exhibited the highest activity for the OER under alkaline conditions among the Co_xFe_yN/graphene samples, showing the lowest overpotential of 266 mV at 10 mA cm^{-2}, the highest current density of 105.83 mA cm^{-2} at 1.53 V, and the lowest Tafel slope of 32 mV dec^{-1}. Moreover, the freestanding electrodes of Co_xFe_yN/graphene catalysts loaded on carbon paper (CP) also exhibited excellent long-term stability for the OER, and the overpotentials only slightly increased after continuously testing for 16 h at 10 mA cm^{-2}. Among all the Co_xFe_yN/graphene/CP samples, the Co_3Fe_1N/graphene/CP sample also displayed the best long-term stability and the lowest overpotential (270 mV) after 16 h. This work presents the great potential of Co_xFe_yN/graphene catalysts as promising non-noble metal electrocatalysts for the OER for application in clean energy conversion devices.

Received 3rd February 2019
Accepted 21st April 2019

DOI: 10.1039/c9ta01347d

rsc.li/materials-a

1. Introduction

In recent years, the oxygen evolution reaction (OER) has drawn great research attention, attributed to its distinguishing characteristics in energy conversion and storage technologies, such as electrocatalytic water splitting devices,[1–4] metal–air batteries[5,6] and electrochemical CO_2 reduction systems.[7] However, the OER process is usually subjected to its multi-proton-coupled electron transfer steps, causing very sluggish reaction kinetics and high overpotential.[8,9] Thus, the development of an effective electrocatalyst to promote the reaction rate is necessary. Up to now, the most efficient electrocatalysts for the OER are still noble metal oxides, such as IrO_2 and RuO_2.[10–15] However, the rareness and high costs of noble metals severely hinder their commercial application. Therefore, it is highly desirable to develop advanced electrocatalysts based on non-noble metal materials with low overpotential and superior stability.

Over the past few years, owing to the unique electron structure and special e_g orbitals, nickel and cobalt based materials have been widely investigated as promising non-noble catalysts for the OER. Especially, layered double hydroxides (LDHs) and metal oxides containing Fe, Co, or Ni species have been regarded as promising OER catalysts.[16–27] However, an intrinsic disadvantage of Ni or Co based LDHs and metal oxides is their poor electron conductivity. These materials are normally semiconducting or insulating, which hinders the electron transfer from the electrocatalysts to the support electrode, thereby greatly limiting the catalytic efficiency. Compared with Ni or Co-based oxides and hydroxides, their metal nitrides exhibit high activity for the OER, attributed to their high electrical conductivity and good electrocatalytic stability.[28–30] Recently, great efforts have been focused on the exploration of metal nitride catalysts, such as Ni_3N nanosheets,[28] Ni_3FeN nanosheets,[31] 3D porous NiCoN,[29] and Co_4N nanowires,[30] for the OER. Moreover, density functional theory (DFT) calculations demonstrate that

[a]Key Laboratory of Mesoscopic Chemistry of MOE, Jiangsu Key Laboratory of Advanced Organic Materials, School of Chemistry and Chemical Engineering, Nanjing University, Nanjing 210023, China. E-mail: zhongjin@nju.edu.cn

[b]Shenzhen Research Institute of Nanjing University, Shenzhen 518063, China

† Electronic supplementary information (ESI) available. See DOI: 10.1039/c9ta01347d

the metallic characteristics of metallic nitrides result from the density of states across the Fermi level.[30]

It is known that doping Fe element in $Ni(OH)_2$ and NiOOH may boost the electrocatalytic activity for the OER,[3,16,32–34] because the partial substitution of Fe element may affect the local electronic structure of Ni-based materials, and the introduction of Fe heteroatoms can increase the number of active sites and enhance the charge-transfer kinetics between Ni and Fe sites.[35] Similarly, with the substitution of Fe ions into Co_3O_4, the OER activity is significantly improved and the Tafel slope is decreased.[36] In Fe mixed Co-based catalysts, Co-based materials can serve as the electrically conductive and chemically stable hosts to enhance the activity of Fe active sites.[37] We suppose that bimetallic nitrides may exhibit even better OER activity than single metal nitrides, because the valence and electronic states of the metal elements could be finely tuned. Furthermore, with the introduction of other metal species, the structure disorder would be increased, thus providing more active sites for the OER.

Following this line of thought, here we demonstrate the preparation of Co_xFe_yN nanoparticles uniformly loaded on graphene nanosheets (Co_xFe_yN/graphene) as efficient electrocatalysts, which can exhibit amazing OER activity and stability as a result of the intrinsic metallic characteristics. The Co_xFe_yN/graphene electrocatalysts were synthesized by the thermal ammonolysis of ultrathin Co_xFe_y-LDH nanosheets loaded on graphene nanosheets. The graphene nanosheets with a two-dimensional (2D) conductive architecture can prevent the aggregation of Co_xFe_yN nanoparticles,[38] and promoted ion diffusion and electron transfer;[39] therefore the active surface area and electrocatalytic activity of the catalysts can be greatly improved. Moreover, with Fe element doping, the disorder degree of the crystalline structure is increased, thus forming a unique electronic structure for extraordinarily high electrocatalytic activity. This work illustrates that the Co_3Fe_1N/graphene catalyst is a promising non-noble metal electrocatalyst for the OER in energy conversion devices (Table S1†). We further anchored the Co_xFe_yN/graphene samples onto conductive carbon paper (Co_xFe_yN/graphene/CP) to prevent the exfoliation of catalysts by oxygen bubbles generated during long-term testing. The Co_xFe_yN/graphene/CP electrodes exhibit excellent long-term stability, with the overpotentials only increasing by ~5 mV during the continuous test from 4 to 16 h at 10 mA cm^{-2}. Among all the Co_xFe_yN/graphene/CP samples, the Co_3Fe_1N/graphene/CP electrode still displays the best activity for the OER, with the lowest overpotential of 270 mV.

2. Experimental section

2.1 Chemicals

All chemicals were of analytical grade and were bought from Sinopharm Chemical Reagent Corp. and used without further purification.

2.2 Preparation of graphene nanosheets

Firstly, graphene oxide (GO) nanosheets were synthesized with natural graphite flakes by a modified Hummers' method.[40] Then, 30 mg GO was dissolved in 50 mL deionized water and stirred for 10 min, and excess $NaBH_4$ was put into the solution to reduce GO and obtain graphene nanosheets. The mixture was stirred for 2 h to decompose the remaining $NaBH_4$, and then the pH of the solution was tuned to neutral by adding 0.1 M HNO_3. A suitable amount of ethanol was added into the solution ($V_{H_2O} : V_{EtOH} = 9 : 1$) and then ultrasonicated for 5 min to form a homogeneous suspension.

2.3 Preparation of ultrathin Co_xFe_y-LDH/graphene nanosheets

In a typical procedure, the prescribed amounts of $Co(NO_3)_2 \cdot 6H_2O$ and $Fe(NO_3)_3 \cdot 9H_2O$ with a mole number of 2.0 mmol were added into the above-prepared graphene suspension. For the preparation of different samples, the ratios of Co^{2+} and Fe^{3+} were adjusted to 4 : 0, 3.6 : 0.4, 3 : 1, 2 : 2, 1 : 3, and 0 : 1, respectively. Triethanolamine (TEA) with a mole number 3 times higher than that of Fe^{3+} was added into the mixture. Then, 16 mmol of hexamethylenetetramine (HMT) were added to the mixture and stirred for 0.5 h. The mixture was sealed into a stainless-steel Teflon-lined autoclave, maintained at 95 °C for 3 h and then cooled down naturally to room temperature. The products were collected by centrifugation at 3000 rpm for 5 min, washed with ethanol and deionized water several times, and then freeze-dried under vacuum at −40 °C overnight.

2.4 Preparation of Co_xFe_yN/graphene samples

The Co_xFe_y-LDH/graphene nanosheets were placed in a tube furnace, heated to 600 °C under 200 sccm N_2 flow with a heating rate of 3 °C min^{-1}, and maintained at this temperature for 3 h with a continuous NH_3 flow of 150 sccm. Then, the tube furnace was cooled down to room temperature under 200 sccm N_2 flow.

2.5 Characterization

The morphology and compositions of the products were characterized by transmission electron microscopy (TEM, JEM-2100), scanning electron microscopy (SEM, Hitachi-S4800) and energy-dispersive X-ray spectroscopy (EDX) coupled with SEM. The samples were characterized by X-ray diffraction (XRD, Bruker D8 Advance A25) using a Co Kα ($\lambda = 1.78897$ Å) radiation source with an Fe filter of 0.02 mm thickness. X-ray photoelectron spectra (XPS) were obtained using a PHI-5000 VersaProbe X-ray photoelectron spectrometer with an Al Kα X-ray radiation source. Inductively coupled plasma optical emission spectroscopy (ICP-OES) was performed on an Optima 5300DV, and the samples were dissolved in dilute nitric acid before testing.

2.6 Electrochemical measurements

Typically, 8.0 mg of Co_xFe_yN/graphene catalysts were dispersed in a 1.0 mL mixed solvent of ethanol and deionized water ($V_{ethanol} : V_{H_2O} = 9 : 1$) comprising 80 μL Nafion (5%), and then ultrasonicated for 0.5 h. The mixture was dropped onto a glassy carbon (GC) based rotating disk electrode (RDE) of 5 mm diameter with a mass loading of 0.2 mg cm^{-2}. Alternatively, to prepare free-standing Co_xFe_yN/graphene/CP electrodes, the

catalyst inks were dropped onto conductive CP (1 × 1 cm) with a mass loading of 0.5 mg cm^{-2}. The electrochemical measurements were performed in a standard three-electrode reaction cell connected to an electrochemical workstation (Chenhua CHI-760E). The electrolyte was 1.0 M KOH solution. Pt foil was used as the counter electrode. The reference electrode was a Hg/HgO electrode (MMO) filled with 1.0 M KOH. Prior to tests, high-purity N_2 was bubbled through the electrolyte to eliminate dissolved O_2, and cyclic voltammetry (CV) was performed between 0 and 0.7 V *vs.* MMO at a scan rate of 200 mV s^{-1} for 30 cycles to clean the surface of the catalysts.

For OER tests, 1.0 M KOH electrolyte was first bubbled by O_2 flow to ensure the O_2/H_2O equilibrium potential at 1.23 V *vs.* the reversible hydrogen electrode (RHE), and then linear sweep voltammetry (LSV) was carried out with a GC based RDE at a rotating speed of 1600 rpm at a scan rate of 10 mV s^{-1} between 0 and 0.7 V *vs.* MMO. The LSV analysis of Co_xFe_yN/graphene/CP electrodes was also carried out between 0 and 0.7 V *vs.* MMO. The percentage of *iR* compensation was 80%, according to the equation $E = E_0 - iR \times 80\%$, where E is the *iR*-corrected potential, E_0 is the potential before *iR* correction, i is the current density, and R is the solution resistance. The activity of the catalysts was normalized by their geometric areas. The electrochemically active surface area (ECSA) was also estimated by the electrochemical double-layer capacitance (C_{dl}), which was investigated on the basis of CV curves recorded at different scan rates from 5 to 100 mV s^{-1} in the non-faradaic potential region. And the value of C_{dl} was computed using the equation $i_c = vC_{dl}$.[29] Chronopotentiometric measurements were recorded at a current density of 10 mA cm^{-2}. The obtained potentials (*vs.* MMO) were converted to potentials *vs.* RHE using the Nernst equation:

$$\begin{aligned} E_{RHE} &= E_{MMO} + 0.059pH + E^0_{MMO} \\ &= E_{MMO} + 0.059pH + 0.098V \end{aligned} \quad (1)$$

and the overpotentials were calculated as below:

$$\begin{aligned} \eta &= E_{MMO} + 0.059pH + E^0_{MMO} - 1.23V \\ &= E_{MMO} + 0.059pH + 0.098V - 1.23V \end{aligned} \quad (2)$$

3. Results and discussion

3.1 Preparation and characterization of the Co_xFe_yN/graphene catalysts

The experimental process for the preparation of Co_xFe_yN/graphene catalysts is detailed in the Experimental section. Firstly, ultrathin Co_xFe_y-LDH nanosheets were easily synthesized by a solution-phase method, which can easily control the atomic proportions of Co and Fe species. In this way, Co_xFe_y-LDH nanosheets with different $x : y$ ratios (from 4 : 0, 3.6 : 0.4, 3 : 1, 2 : 2, and 1 : 3 to 0 : 4) were prepared to compare the variation of electrocatalytic properties. To prevent the aggregation and enhance the conductivity of ultrathin LDH nanosheets, graphene nanosheets were added into the reaction vessel to obtain Co_xFe_y-LDH/graphene composites, as shown in Fig. S1.† Through the adding of graphene, the specific surface area, the number of exposed active sites, and the charge transfer properties of the products can be greatly increased. Subsequently, the ultrathin Co_xFe_y-LDH nanosheets were converted to Co_xFe_yN nanoparticles and decorated on graphene *via* thermal treatment in an NH_3 atmosphere at 600 °C for 3 h, as shown in Fig. 1a–f. Scanning electron microscopy (SEM) images show that the Co_xFe_yN nanoparticles are loaded on the surface of graphene uniformly. With the increase of Fe content, the average diameter of Co_xFe_yN nanoparticles also increased from about 10 nm to 30 nm. As presented in Fig. 1g–l, the high-resolution transmission electron microscopy (HRTEM) images show the clear crystalline lattices of Co_xFe_yN nanoparticles. In Fig. 1g, the lattice spacing was measured to be 0.2247 nm, which was indexed to the (111) planes of Co_4N.[30,41] Fig. 1h exhibits the (111) plane spacing of $Co_{3.6}Fe_{0.4}N$ (0.2290 nm), which is slightly narrower than that of Co_4N owing to the introduction of Fe atoms. As the atomic ratio of Co and Fe further decreased from 3 : 1 to 2 : 2, 1 : 3 and 0 : 4 (Fig. 1i–l), the crystalline phase of the samples matched with Fe_8N (JCPDF: 89-7097) instead of Co_4N, and the lattice fringes were indexed to (220) planes. With the increase of Fe content, the (220) lattice spacings of these four samples become broader, in accordance with the XRD results in Fig. 2a and b. We also prepared a control sample of Co_3Fe_1N without graphene by treating pristine Co_3Fe_1-LDH in an NH_3 atmosphere at 600 °C for 3 h, and it would aggregate and turn into large particles (Fig. S2†). This indicates that the introduction of graphene can efficiently prevent the aggregation of Co_xFe_yN nanoparticles.

The X-ray diffraction (XRD) pattern of Co_4N/graphene and $Co_{3.6}Fe_{0.4}N$/graphene samples exhibit typical diffraction peaks at around 52.0° and 60.3° (Fig. 2a and b), corresponding to the (111) and (200) planes of Co_4N, respectively. As the Co/Fe ratio changed from 4 : 0 to 3 : 1, the XRD peaks of Co_4N(111) and (200) planes moved to lower angles and became weaker. Finally, the peaks of Co_4N (111) and (200) planes disappeared in the XRD spectrum of the Co_2Fe_2N/graphene sample. In contrast, the peaks corresponding to Fe_8N (220) and (440) planes first appeared in the XRD spectrum of the Co_3Fe_1N/graphene sample, indicting the mixed crystalline phases of this sample. This peak moved to lower angles and became stronger when the Co/Fe ratio further decreased from 3 : 1 to 0 : 4, which demonstrates that the change of Fe content in Co_xFe_yN nanoparticles can greatly influence the lattice spacings and degree of crystallinity. Specifically, for the Fe_4N/graphene sample, the strong peaks at 52.5° and 77.4° are indexed to the (220) and (440) planes of Fe_8N (JCPDF: 89-7097), respectively; the weak peaks at 48.2° and 50.7° can be indexed to the (002) and (101) planes of Fe_3N (JCPDF: 01-1236), respectively; the weak peak at 56.2° corresponds to the (200) planes of $Fe_{4.4}N$ (JCPDF: 03-0955). Therefore, it reveals that the Fe_4N/graphene sample actually contains a mixture of Fe_3N, Fe_8N and $Fe_{4.4}N$.

The compositions of the Co_xFe_yN/graphene catalysts were identified by energy dispersive X-ray spectroscopy (EDX, Fig. S3†) and ICP-OES (Table S2†), which revealed the presence of Co, Fe and N elements, and the ratios of Co and Fe atoms

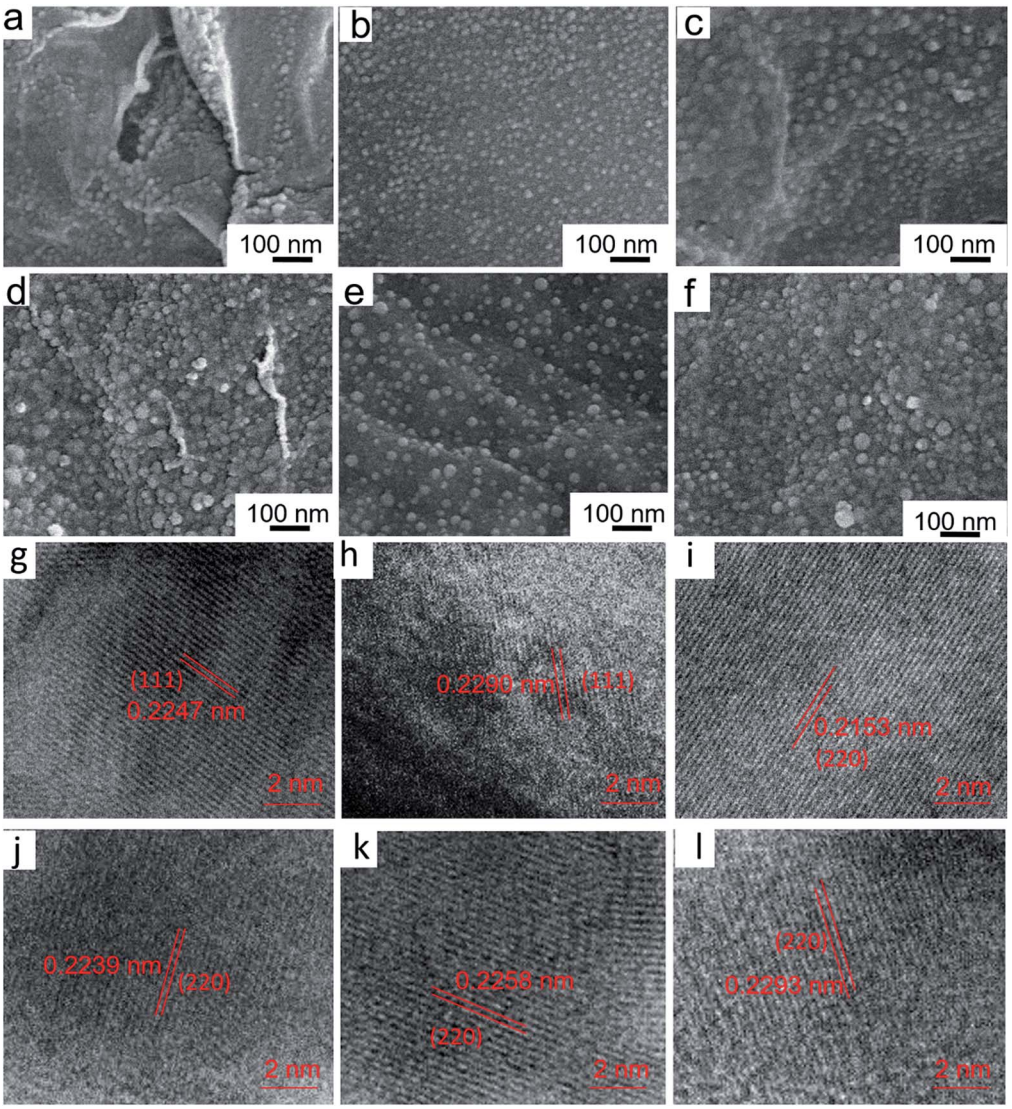

Fig. 1 (a–f) SEM and (g–l) HRTEM images of the as-prepared Co_xFe_yN/graphene samples: (a, g) Co_4N/graphene, (b, h) $Co_{3.6}Fe_{0.4}N$/graphene, (c, i) Co_3Fe_1N/graphene, (d, j) Co_2Fe_2N/graphene, (e, k) Co_1Fe_3N/graphene and (f, l) Fe_4N/graphene, respectively.

were in accordance with the molar proportions of the initial reactants. The chemical valence states of the samples were examined by X-ray photoelectron spectroscopy (XPS). In the Co 2p region (Fig. 2c and S5†), the peaks at around 779.0 eV and 794.5 eV are attributed to Co $2p_{3/2}$ and Co $2p_{1/2}$, respectively, and the peaks at around 785.6 and 801.0 eV are satellite peaks. The peaks at approximately 780.0 eV and 795.2 eV are assigned to Co(+2),[41] and the peaks at around 778.3 eV and 793.4 eV are in accordance with those of Co(0)[26,29,41] reduced during thermal ammonolysis.[28,29] In the Fe 2p region (Fig. 2d and S5†), the peaks at approximately 709.0 eV and 723.0 eV are assigned to Fe $2p_{3/2}$ and Fe $2p_{1/2}$, respectively, while the peak at around 719.0 eV is the satellite peak. The peaks at approximately 710.2 and 724.3 eV are assigned to Fe(+3), and the peaks at approximately 709.0 eV and 722.0 eV are ascribed to Fe(0).[31] In the N 1s XPS spectra (Fig. S4 and S7†), the peaks located at 397.8, 399.0 and 396.6 eV are assigned to the N species in metal nitrides.[41,42] The control sample of pristine graphene treated at 600 °C under an ammonia atmosphere for 3 h shows no sign of N doping, as presented in the EDX spectrum (Fig. S8†). This indicates that no obvious nitrogen doping has occurred on graphene sheets, because previous research studies have revealed that doping nitrogen into graphene by ammonia treatment normally happens at temperatures above 900 °C.[43–45] Therefore, the influence of N-doping in graphene on the OER performance of the Co_xFe_yN/graphene samples is minimal and can be ignored.

3.2 Electrocatalytic performance of the Co_xFe_yN/graphene catalysts for the OER

The electrocatalytic activity of the Co_xFe_yN/graphene catalysts for the OER was investigated in a standard three-electrode system with O_2 saturated 1.0 M KOH solution (as detailed in the ESI†). During the OER tests, the rotating speed of the RDE was maintained at 1600 rpm to remove oxygen bubbles

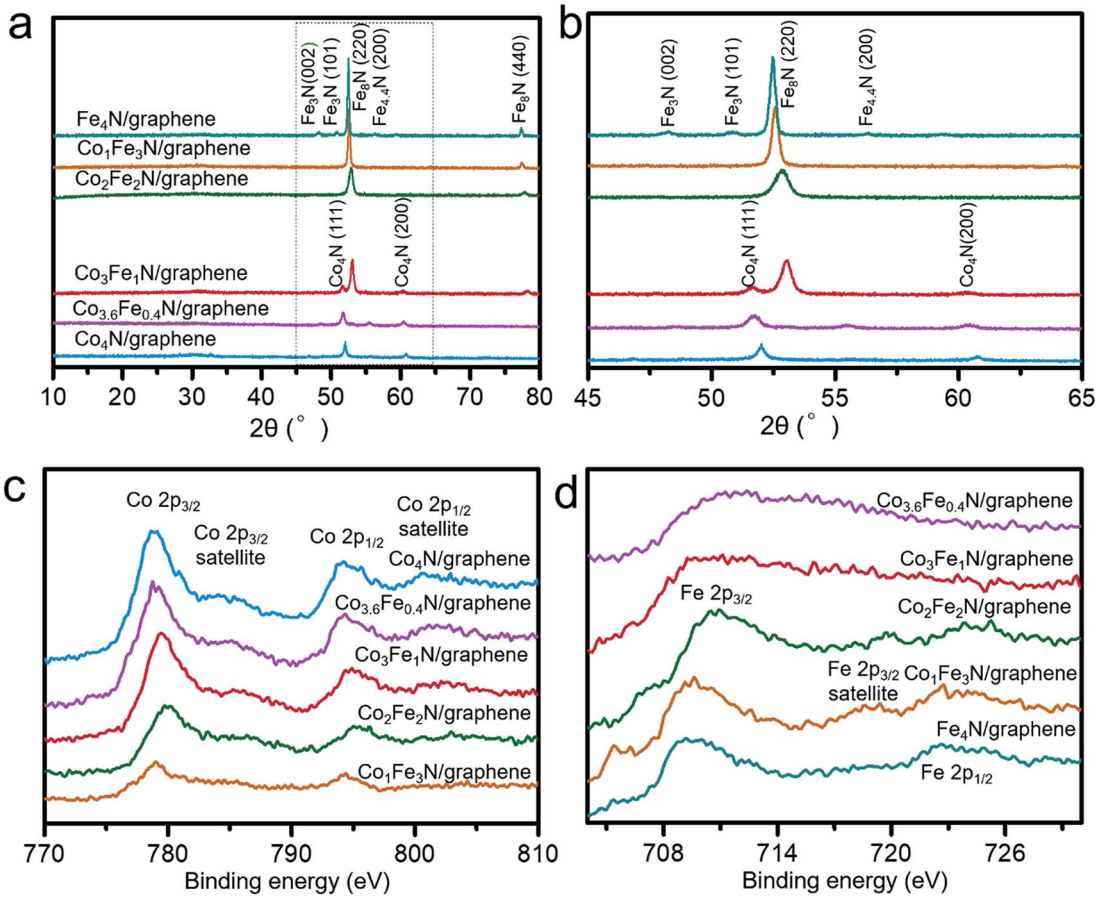

Fig. 2 (a, b) XRD spectra of the Co_xFe_yN/graphene samples. (b) shows the magnification of (a) in the diffraction angle range of 45–65°. (c, d) High-resolution XPS spectra in the Co 2p and Fe 2p regions of the Co_xFe_yN/graphene samples, respectively.

generated by the catalysts. As presented in Fig. 3a–c, the *iR*-corrected OER polarization curves were recorded at a scan rate of 10 mV s^{-1}. The current density was normalized by the geometric area of the electrode. Among all of the Co_xFe_yN/graphene catalysts, the Co_3Fe_1N/graphene sample exhibited the lowest overpotential of 266 mV at 10 mA cm^{-2}, making it superior to Co_4N/graphene (336 mV), $Co_{3.6}Fe_{0.4}N$/graphene (283 mV), Co_2Fe_2N/graphene (310 mV), Co_1Fe_3N/graphene (370 mV), and Co_3Fe_1N (350 mV). The current density of the Fe_4N/graphene sample cannot reach 10 mA cm^{-2} in the testing potential range, indicating its low electrocatalytic activity. At a fixed potential of 1.53 V *vs.* RHE (corresponding to an overpotential of 300 mV), the current density of the Co_3Fe_1N/graphene sample is 105.83 mA cm^{-2}, much higher than those of Co_4N/graphene (5.04 mA cm^{-2}), $Co_{3.6}Fe_{0.4}N$/graphene (30.26 mA cm^{-2}), Co_2Fe_2N/graphene (7.00 mA cm^{-2}), Co_1Fe_3N/graphene (0.26 mA cm^{-2}), Fe_4N/graphene (0.74 mA cm^{-2}) and Co_3Fe_1N (0.71 mA cm^{-2}). Among all of the Co_xFe_yN/graphene samples, Co_3Fe_1N/graphene exhibits the largest C_{dl} value (Fig. S9 and S10†), meaning the largest electrochemically active surface area, and it would contribute to the enhancement of electrochemical activity. Compared to Co_3Fe_1N/graphene, the control sample of Co_3Fe_1N without graphene shows inferior electrocatalytic activity (Fig. 3a). This result confirms that the graphene support with a 2D conductive architecture can increase the specific surface area and boost the electron transfer capability of Co_xFe_yN catalysts, thus improving the OER performance.[39] As presented in Fig. 3b, the magnified OER polarization curve of Co_4N/graphene shows two peaks at about 1.03 V and 1.10 V, which are attributed to the oxidation of surface Co species into CoOOH and then CoO_2.[46,47] With the introduction of Fe atoms, the Co oxidation peaks of $Co_{3.6}Fe_{0.4}N$/graphene and Co_3Fe_1N/graphene shifted to higher potentials, revealing that the incorporation of Fe atoms greatly changed the electronic structure of the Co_xFe_yN based catalysts. This indicates that the strong interactions between Co and Fe atoms could improve the electrochemical stability of surface Co(+2) and Co(0) species, and make the Co oxidation more difficult.[37] However, as the Fe content further increases to ≥50%, the Co oxidation peaks in the OER polarization curves of Co_2Fe_2N/graphene, Co_1Fe_3N/graphene and Fe_4N/graphene samples will disappear and the electrocatalytic activity will decrease. This should be ascribed to the coverage decrease of surface Co species and the variation of the crystalline phase, which is well consistent with the disappearance of the XRD peaks of the Co_4N phase in the Co_2Fe_2N/graphene sample (Fig. 2a and b).

As shown in Fig. 3d, the Tafel slope of the Co_3Fe_1N/graphene sample is 32 mV dec^{-1}, which is lower than those of $Co_{3.6}Fe_{0.4}N$/

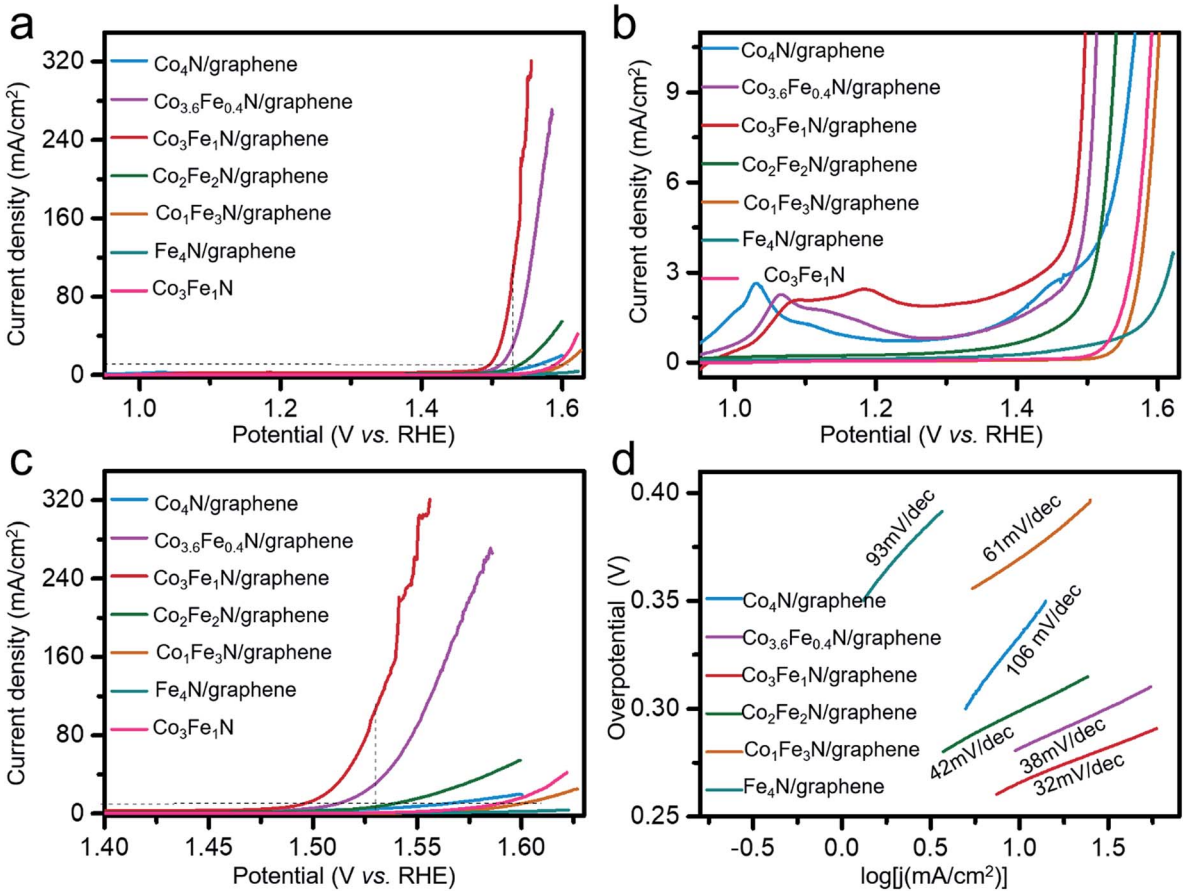

Fig. 3 (a) OER polarization curves of the Co_xFe_yN/graphene catalysts and Co_3Fe_1N without the graphene catalyst after *iR*-correction. (b) and (c) are the magnified rectangular parts in (a) at low current densities and at high potentials, respectively. (d) Tafel plots of the Co_xFe_yN/graphene catalysts recorded at a scan rate of 10 mV s^{-1} in O_2 saturated 1.0 M KOH solution.

graphene (38 mV dec^{-1}), Co_2Fe_2N/graphene (42 mV dec^{-1}), Co_1Fe_3N/graphene (61 mV dec^{-1}), Fe_4N/graphene (93 mV dec^{-1}) and Co_4N/graphene (106 mV dec^{-1}). The lowest onset potential and Tafel slope confirm that the Co_3Fe_1N/graphene sample has the highest OER activity among all of the Co_xFe_yN/graphene samples. The Tafel plot is normally used to deduce the rate-limiting factors in the four electron transfer steps of the OER, as illustrated by the classical Butler–Volmer equation below:[37]

$$\text{Tafel slope (mV dec}^{-1}) = 59/(n' + \alpha) \quad (3)$$

where n' is the number of single-electron transfer steps prior to the rate-determining step and α is the symmetry/transfer coefficient (typically taken as 0.5). It has been predicted that the Tafel slopes close to 24 mV dec^{-1} and 40 mV dec^{-1} indicate that the third electron transfer and the second electron transfer are the rate-determining steps, respectively. And the Tafel slope near 60 mV dec^{-1} is related to a rate-limiting step following the first electron transfer. In Fig. 3d, the Tafel slope of the Co_3Fe_1N/graphene sample is 32 mV dec^{-1}, which is between 24 mV dec^{-1} and 40 mV dec^{-1}; we thus conclude that both the second electron transfer and the third electron transfer are the rate-limiting factors. The Tafel slopes of $Co_{3.6}Fe_{0.4}N$/graphene and Co_2Fe_2N/graphene are 38 mV dec^{-1} and 42 mV dec^{-1}, respectively, which are near 40 mV dec^{-1}, indicating that the second electron transfer is the rate-determining step. The Tafel slope of the Co_1Fe_3N/graphene sample (61 mV dec^{-1}) is near 60 mV dec^{-1}, verifying that the first electron transfer followed by chemical absorption is the rate-limiting step.[46]

Notably, despite the similar catalyst configuration, the Co_3Fe_1N/graphene sample shows the lowest Tafel slope among all of the samples, which could be attributed to the optimal charge transfer on the catalyst surface. It has been revealed that transition metal nitrides usually have better conductivity and corrosion resistance compared to the corresponding metal oxides and hydroxides.[28] DFT calculation studies also indicate the metallic characteristics of transition metal nitrides, owing to the density of states (DoS) across the Fermi level.[28,30,42] This is in accordance with the XPS results of the Co_xFe_yN/graphene samples, which confirms that the Co species is in the Co(+2) and Co(0) states, and the Fe species is in the Fe(+3) and Fe(0) states. Benefitting from the intrinsic metallic character of Co_xFe_yN nanoparticles and the good conductivity of graphene sheets, the Co_xFe_yN/graphene catalysts exhibit fast charge transport properties and high catalytic activity. Moreover, the highest OER activity of the Co_3Fe_1N/graphene sample indicates

that the composition optimization of the metal nitride catalyst is a feasible way to improve the catalytic activity for the OER. Compared with Co_4N/graphene and Fe_4N/graphene, the other bimetallic Co_xFe_yN/graphene samples also show better electrocatalytic activity. These results indicate that the incorporation of Fe ions into Co_xFe_yN can greatly influence the chemical valences and electronic states of the catalyst to create more active sites and facilitate rapid charge transfer, thus boosting the electrocatalytic activity. On the other hand, the reaction kinetics of the OER could be promoted by the graphene sheets serving as a conductive support, which provides smooth pathways for electron transport and prevents the aggregation of Co_xFe_yN nanoparticles. In brief, the improved catalytic performance should be attributed to the synergistic effect of introduced Fe species and 2D graphene support.

3.3 Electrocatalytic performance of the free-standing Co_xFe_yN/graphene/CP electrodes for the OER

Apart from the electrocatalytic activity, the stability of the catalyst is also an important factor for practical applications. During long-term chronopotentiometric tests, the Co_xFe_yN/graphene catalysts attached on GC based RDEs may be stripped off due to the generation of a large number of O_2 bubbles. Therefore, we loaded the Co_xFe_yN/graphene catalysts on carbon paper (CP) to form free-standing Co_xFe_yN/graphene/CP electrodes with a large surface area, high conductivity and good adhesion, which can efficiently prevent the exfoliation of catalysts by O_2 bubbles. The OER performances of the Co_xFe_yN/graphene/CP electrodes were systematically measured in O_2 saturated 1.0 M KOH solution (Fig. 4). The *iR*-corrected OER polarization curves of the Co_xFe_yN/graphene/CP electrodes (Fig. 4a) showed similar trends compared to those of Co_xFe_yN/graphene catalysts loaded on GC electrodes. The Co_3Fe_1N/graphene/CP electrode exhibited the highest OER activity among all the electrodes, delivering an overpotential (270 mV at 20 mA cm^{-2}) lower than Co_4N/graphene/CP (336 mV), $Co_{3.6}Fe_{0.4}N$/graphene/CP (291 mV), Co_2Fe_2N/graphene/CP (309 mV), Co_1Fe_3N/graphene/CP (347 mV) and Fe_4N/graphene/CP (>400 mV). At a fixed potential of 1.53 V *vs.* RHE (corresponding to an overpotential of 300 mV), the current density of the Co_3Fe_1N/graphene/CP electrode is measured to be 73.47 mA cm^{-2}, which is much higher than those of Co_4N/graphene/

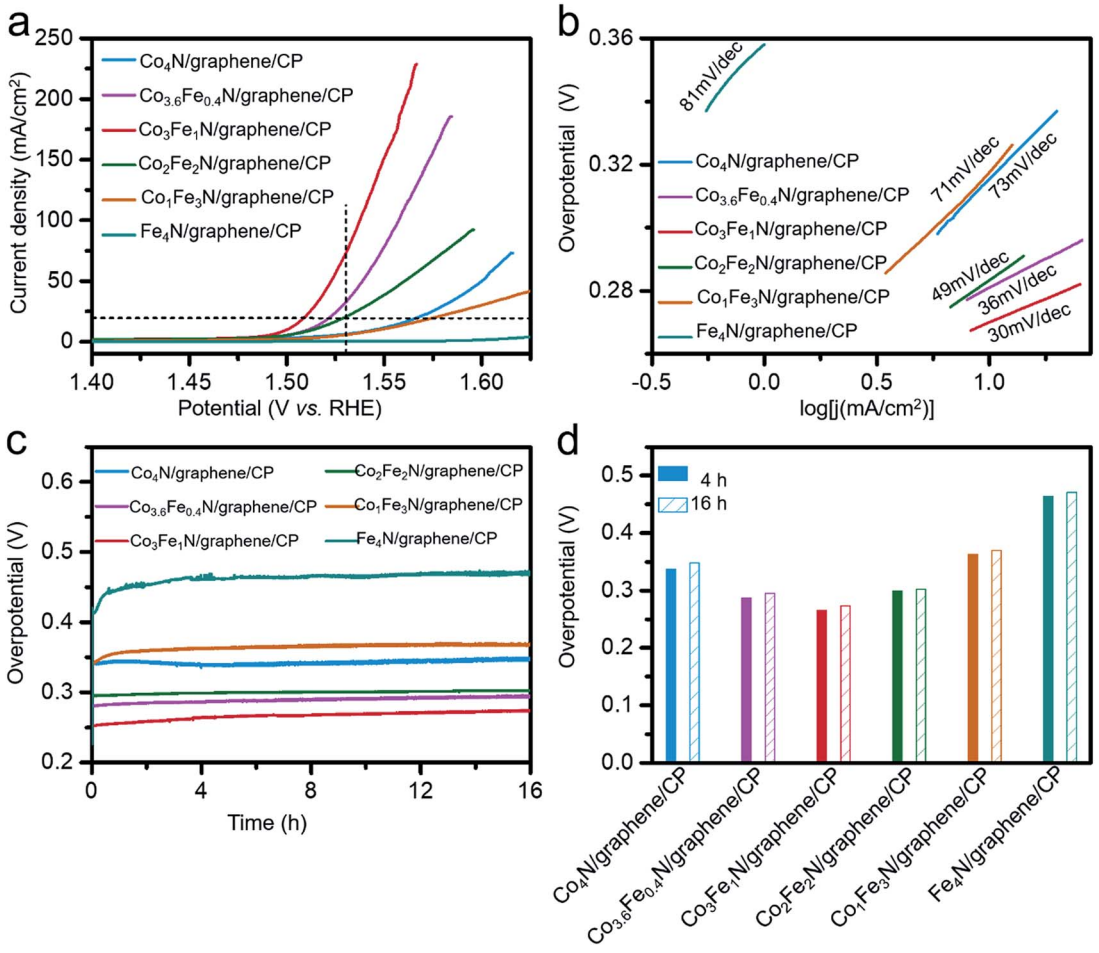

Fig. 4 (a) The *iR*-corrected OER polarization curves and (b) Tafel plots of the free-standing Co_xFe_yN/graphene/CP electrodes recorded at a scan rate of 5 mV s^{-1} in O_2 saturated 1.0 M KOH solution. (c) Chronopotentiometric measurements of the Co_xFe_yN/graphene/CP electrodes recorded at 10 mA cm^{-2}. (d) The overpotentials obtained from (c) after continuous testing for 4 h (solid columns) and 16 h (patterned columns).

CP (6.33 mA cm^{-2}), $Co_{3.6}Fe_{0.4}N$/graphene/CP (33.58 mA cm^{-2}), Co_2Fe_2N/graphene/CP (20.51 mA cm^{-2}), Co_1Fe_3N/graphene/CP (5.55 mA cm^{-2}) and Fe_4N/graphene/CP (0.28 mA cm^{-2}). The catalytic activity of the Co_xFe_yN/graphene/CP electrodes at high potential could be ranked in the following order: Co_3Fe_1N/graphene/CP > $Co_{3.6}Fe_{0.4}N$/graphene/CP > Co_2Fe_2N/graphene/CP > Co_4N/graphene/CP ≈ Co_1Fe_3N/graphene/CP > Fe_4N/graphene/CP. The current densities of the Co_xFe_y N/graphene/CP electrodes are slightly lower than those of the Co_xFe_y N/graphene loaded GC electrodes, which is because the generated O_2 bubbles cannot be immediately removed from the catalyst surface without the rotation of RDEs. The Tafel plots of all samples obtained from the polarization curves are presented in Fig. 4b. The Tafel slope of Co_3Fe_1N/graphene/CP (30 mV dec^{-1}) is lower than those of Co_4N/graphene/CP (73 mV dec^{-1}), $Co_{3.6}Fe_{0.4}N$/graphene/CP (36 mV dec^{-1}), Co_2Fe_2N/graphene/CP (49 mV dec^{-1}), Co_1Fe_3N/graphene/CP (71 mV dec^{-1}) and Fe_4N/graphene/CP (81 mV dec^{-1}). Owing to the good dispersion of catalyst nanoparticles on the conductive CP support, the Tafel slopes of the Co_xFe_yN/graphene/CP electrodes are slightly lower than those measured with GC based RDEs. To investigate the performance stability, long-term chronopotentiometric tests of the Co_xFe_yN/graphene/CP electrodes were carried out (Fig. 4c), showing well-maintained overpotentials in the continuous tests of 16 h. There were only a few fluctuations during the testing process, owing to the adsorption, accumulation and desorption of O_2 bubbles on the electrode surface. The overpotentials of all samples after testing for 4 h and 16 h are compared in Fig. 4d, which shows that the overpotentials of the Co_xFe_yN/graphene/CP electrodes only increased by about 5 mV. It can be concluded that the Co_xFe_yN/graphene/CP electrodes exhibited good long-term stability in alkaline solution. Among all the electrodes, the Co_3Fe_1N/graphene/CP electrode retained the best activity after long-time OER testing, with the lowest overpotential of 270 mV at 10 mA cm^{-2}.

4. Conclusions

In summary, we have synthesized a series of Co_xFe_yN/graphene catalysts with controlled morphology and compositions through the thermal ammonolysis of ultrathin Co_xFe_y-LDH nanosheets grown on graphene. Owing to the intrinsic metallic characteristics and the electronic structure modification by Fe atoms, the Co_xFe_yN/graphene catalysts exhibited improved electrocatalytic activity for the OER. Among the samples with different Co/Fe ratios, the Co_3Fe_1N/graphene sample showed the lowest overpotential and Tafel slope. Moreover, the Co_xFe_yN/graphene/CP electrodes also demonstrated remarkable stability during long-term OER tests. This work provides a promising route to prepare high-performance hybrid electrocatalysts based on non-noble metal nitrides for the OER for application in clean energy conversion devices.

Conflicts of interest

There are no conflicts to declare.

Acknowledgements

This work was supported by the National Key R&D Program of China (2017YFA0208200, 2016YFB0700600, and 2015CB659300), Projects of NSFC (21802068, 21872069, 51761135104, and 21573108), Natural Science Foundation of Jiangsu Province (BK20180008 and BK20160643), High-Level Entrepreneurial and Innovative Talents Program of Jiangsu Province, and the Fundamental Research Funds for the Central Universities of China.

Notes and references

1 X. Long, G. Li, Z. Wang, H. Zhu, T. Zhang, S. Xiao, W. Guo and S. Yang, *J. Am. Chem. Soc.*, 2015, **137**, 11900–11903.
2 C. L. Xiao, X. Y. Lu and C. Zhao, *Chem. Commun.*, 2014, **50**, 10122–10125.
3 M. W. Louie and A. T. Bell, *J. Am. Chem. Soc.*, 2013, **135**, 12329–12337.
4 Q. Li, X. Wang, K. Tang, M. Wang, C. Wang and C. Yan, *ACS Nano*, 2017, **11**, 12230–12239.
5 X. Liu, M. Park, M. G. Kim, S. Gupta, G. Wu and J. Cho, *Angew. Chem., Int. Ed.*, 2015, **54**, 9654–9658.
6 Z. Cui, G. Fu, Y. Li and J. B. Goodenough, *Angew. Chem.*, 2017, **129**, 10033–10037.
7 G. A. Olah, G. K. S. Prakash and A. Goeppert, *J. Am. Chem. Soc.*, 2011, **133**, 12881–12898.
8 R. Subbaraman, D. Tripkovic, K.-C. Chang, D. Strmcnik, A. P. Paulikas, P. Hirunsit, M. Chan, J. Greeley, V. Stamenkovic and N. M. Markovic, *Nat. Mater.*, 2012, **11**, 550–557.
9 Q. Q. Xiao, Y. X. Zhang, X. Guo, L. Jing, Z. Y. Yang, Y. F. Xue, Y. M. Yan and K. N. Sun, *Chem. Commun.*, 2014, **50**, 13019–13022.
10 T. Reier, M. Oezaslan and P. Strasser, *ACS Catal.*, 2012, **2**, 1765–1772.
11 Y. E. Roginskaya, T. V. Varlamova, M. D. Goldstein, I. D. Belova, B. S. Galyamov, R. R. Shifrina, V. A. Shepelin and V. N. Fateev, *Mater. Chem. Phys.*, 1991, **30**, 101–113.
12 N. Danilovic, R. Subbaraman, K. C. Chang, S. H. Chang, Y. Kang, J. Snyder, A. P. Paulikas, D. Strmcnik, Y. T. Kim, D. Myers, V. R. Stamenkovic and N. M. Markovic, *Angew. Chem., Int. Ed.*, 2014, **53**, 1–7.
13 H. N. Nong, L. Gan, E. Willinger, D. Teschner and P. Strasser, *Chem. Sci.*, 2014, **5**, 2955–2963.
14 W. Hu, Y. Wang, X. Hu, Y. Zhou and S. Chen, *J. Mater. Chem.*, 2012, **22**, 6010–6016.
15 W. Hu, H. Zhong, W. Liang and S. Chen, *ACS Appl. Mater. Interfaces*, 2014, **6**, 12729–12736.
16 F. Song and X. L. Hu, *Nat. Commun.*, 2014, **5**, 4477.
17 A. S. Batchellor and S. W. Boettcher, *ACS Catal.*, 2015, 6680–6689.
18 F. Song and X. L. Hu, *J. Am. Chem. Soc.*, 2014, **136**, 16481–16484.
19 J. Huang, J. Chen, T. Yao, J. He, S. Jiang, Z. Sun, Q. Liu, W. Cheng, F. Hu, Y. Jiang, Z. Pan and S. Wei, *Angew. Chem., Int. Ed.*, 2015, **54**, 1–7.

20 D. Friebel, M. W. Louie, M. Bajdich, K. E. Sanwald, Y. Cai, A. M. Wise, M.-J. Cheng, D. Sokaras, T.-C. Weng, R. Alonso-Mori, R. C. Davis, J. R. Bargar, J. K. Nørskov, A. Nilsson and A. T. Bell, *J. Am. Chem. Soc.*, 2015, **137**, 1305–1313.
21 M. Gong, Y. Li, H. Wang, Y. Liang, J. Z. Wu, J. Zhou, J. Wang, T. Regier, F. Wei and H. Dai, *J. Am. Chem. Soc.*, 2013, **135**, 8452–8455.
22 W. W. Xu, Z. Y. Lu, X. D. Lei, Y. P. Li and X. M Sun, *Phys. Chem. Chem. Phys.*, 2014, **16**, 20402–20405.
23 X. Zhou, X. Shen, Z. Xia, Z. Zhang, J. Li, Y. Ma and Y. Qu, *ACS Appl. Mater. Interfaces*, 2015, **7**, 20322–20331.
24 L. Xu, Q. Jiang, Z. Xiao, X. Li, J. Huo, S. Wang and L. Dai, *Angew. Chem., Int. Ed.*, 2016, **55**, 1–6.
25 D. Wang, X. Chen, D. G. Evans and W. Yang, *Nanoscale*, 2013, **5**, 5312–5315.
26 H. Jin, J. Wang, D. Su, Z. Wei, Z. Pang and Y. Wang, *J. Am. Chem. Soc.*, 2015, **137**, 2688–2694.
27 X. Wang, P. Sun, H. Lu, K. Tang, Q. Li, C. Wang, Z. Mao, T. Ali and C. Yan, *Small*, 2019, **15**, 1804886.
28 K. Xu, P. Chen, X. Li, Y. Tong, H. Ding, X. Wu, W. Chu, Z. Peng, C. Wu and Y. Xie, *J. Am. Chem. Soc.*, 2015, **137**, 4119–4125.
29 Y. Wang, B. Zhang, W. Pan, H. Ma and J. Zhang, *ChemSusChem*, 2017, **10**, 4170–4177.
30 P. Chen, K. Xu, Z. Fang, Y. Tong, J. Wu, X. Lu, X. Peng, H. Ding, C. Wu and Y. Xie, *Angew. Chem.*, 2015, **127**, 14923–14927.
31 X. Jia, Y. Zhao, G. Chen, L. Shang, R. Shi, X. Kang, G. I. N. Waterhouse, L.-Z. Wu, C.-H. Tung and T. Zhang, *Adv. Energy Mater.*, 2016, **6**, 1502585.
32 D. Friebel, M. W. Louie, M. Bajdich, K. E. Sanwald, Y. Cai, A. M. Wise, M.-J. Cheng, D. Sokaras, T.-C. Weng, R. Alonso-Mori, R. C. Davis, J. R. Bargar, J. K. Nørskov, A. Nilsson and A. T. Bell, *J. Am. Chem. Soc.*, 2015, **137**, 1305–1313.
33 J. Y. C. Chen, L. Dang, H. Liang, W. Bi, J. B. Gerken, S. Jin, E. E. Alp and S. S. Stahl, *J. Am. Chem. Soc.*, 2015, **137**, 15090–15093.
34 H. Liu, Y. Wang, X. Lu, Y. Hu, G. Zhu, R. Chen, L. Ma, H. Zhu, Z. Tie, J. Liu and Z. Jin, *Nano Energy*, 2017, **35**, 350–357.
35 Y. Xie, X. Wang, K. Tang, Q. Li and C. Yan, *Electrochim. Acta*, 2018, **264**, 225–323.
36 E. Laouini, M. Hamdani, M. I. S. Pereira, J. Douch, M. H. Mendonça, Y. Berghoute and R. N. Singh, *Int. J. Hydrogen Energy*, 2008, **33**, 4936–4944.
37 M. S. Burke, M. G. Kast, L. Trotochaud, A. M. Smith and S. W. Boettcher, *J. Am. Chem. Soc.*, 2015, **137**, 3638–3648.
38 J. Li, M. Yan, X. Zhou, Z.-Q. Huang, Z. Xia, C.-R. Chang, Y. Ma and Y. Qu, *Adv. Funct. Mater.*, 2016, **26**, 6785–6796.
39 D. Li, Q. Liao, B. Ren, Q. Jin, H. Cui and C. Wang, *J. Mater. Chem. A*, 2017, **5**, 11301–11308.
40 D. C. Marcano, D. V. Kosynkin, J. M. Berlin, A. Sinitskii, Z. Sun, A. Slesarev, L. B. Alemany, W. Lu and J. M. Tour, *ACS Nano*, 2010, **4**, 4806–4814.
41 B. Cao, G. M. Veith, J. C. Neuefeind, R. R. Adzic and P. G. Khalifah, *J. Am. Chem. Soc.*, 2013, **135**, 19186–19192.
42 Y.-Z. Li, T.-T. Li, W. Chen and Y.-Y. Song, *ACS Appl. Mater. Interfaces*, 2017, **9**, 29881–29888.
43 X. Li, L. An, X. Chen, N. Zhang, D. Xia, W. Huang, W. Chu and Z. Wu, *Sci. Rep.*, 2013, **3**, 3234.
44 Y. Li, W. Zhou, H. Wang, L. Xie, Y. Liang, F. Wei, J.-C. Idrobo, S. J. Pennycook and H. Dai, *Nat. Nanotechnol.*, 2012, **7**, 394.
45 D. Geng, Y. Chen, Y. Chen, Y. Li, R. Li, X. Sun, S. Ye and S. Knights, *Energy Environ. Sci.*, 2011, **4**, 760–764.
46 Y. Surendranath, M. W. Kanan and D. G. Nocera, *J. Am. Chem. Soc.*, 2010, **132**, 16501–16509.
47 N. H. Chou, P. N. Ross, A. T. Bell and T. D. Tilley, *ChemSusChem*, 2011, **4**, 1566–1569.